Nanoscale

ROYAL SOCIETY OF CHEMISTRY

PAPER

View Article Online
View Journal | View Issue

Cite this: *Nanoscale*, 2023, **15**, 10133

In situ electron tomography for the thermally activated solid reaction of anaerobic nanoparticles†

Shiro Ihara, [a] Mizumo Yoshinaga, [b] Hiroya Miyazaki, [c] Kota Wada, [b] Satoshi Hata, [b,d] Hikaru Saito *[a,e] and Mitsuhiro Murayama [a,f,g]

The nanoscale characterization of thermally activated solid reactions plays a pivotal role in products manufactured by nanotechnology. Recently, *in situ* observation in transmission electron microscopy combined with electron tomography, namely four-dimensional observation for heat treatment of nanomaterials, has attracted great interest. However, because most nanomaterials are highly reactive, *i.e.*, oxidation during transfer and electron beam irradiation would likely cause fatal artefacts; it is challenging to perform the artifact-free four-dimensional observation. Herein, we demonstrate our development of a novel *in situ* three-dimensional electron microscopy technique for thermally activated solid-state reaction processes in nanoparticles (NPs). The sintering behaviour of Cu NPs was successfully visualized and analyzed in four-dimensional space–time. An advanced image processing protocol and a newly designed state-of-the-art MEMS-based heating holder enable the implementation of considerably low electron dose imaging and prevent air exposure, which is of central importance in this type of observation. The total amount of electron dose for a single set of tilt-series images was reduced to 250 e^{-} nm^{-2}, which is the lowest level for inorganic materials electron tomography experiments. This study evaluated the sintering behaviour of Cu NPs in terms of variations in neck growth and particle distance. A negative correlation between the two parameters is shown, except for the particle pair bound by neighbouring NPs. The nanoscale characteristic sintering behavior of neck growth was also captured in this study.

Received 2nd March 2023,
Accepted 9th May 2023

DOI: 10.1039/d3nr00992k

rsc.li/nanoscale

Introduction

It is well known that thermally activated solid-state reaction of materials, especially sintering, is an important process relevant to various industrial products, *e.g.*, catalysts, magnets, and electronic devices.[1] Metal nanoparticles (NPs), such as Ag and Cu, have attracted great attention in printed electronics[2–5] because they can be sintered at relatively low temperatures compared to the bulk state, meaning the NPs are environmentally friendly and enable low-cost manufacturing processes.[6] The electrical conductivity of sintered NPs is affected by the degree of neck growth between adjacent particles. Therefore, clarifying the dominant factor of neck growth is of vital importance for designing NPs and their processing protocols. Several widely used sintering models proposed by Kuczynski,[7] Kingery[8] and Coble[9] provide reasonable predictions for the sintering behaviour of particles with a diameter equal to or greater than a micro-meter, where the effects of surface properties are smaller than those in nanoscale dimensions. In the micro-meter scale, the sintering behaviour of particles can be expressed by a single diffusion mechanism, such as surface diffusion and volume diffusion.[10] In NPs, surface effects become notable owing to their high surface-to-volume ratio, which enhances multiple diffusion mechanisms.[11–13] This nanoscale effect makes it difficult to determine the important factor in describing nanoscale sintering. Thus far, predicting the sintering behaviour of NPs is a challenging issue.

To clarify the sintering behaviour of NPs, tremendous efforts have been made in both experimental and computational approaches. For experimental approaches, *in situ*

[a]*Institute for Materials Chemistry and Engineering, Kyushu University, Fukuoka 816-8580, Japan. E-mail: saito.hikaru.961@m.kyushu-u.ac.jp*
[b]*Interdisciplinary Graduate School of Engineering Sciences, Kyushu University, Fukuoka 816-8580, Japan*
[c]*Mel-Build Corporation, Nishi-ku, Fukuoka 819-0052, Japan*
[d]*The Ultramicroscopy Research Center, Kyushu University, Fukuoka 819-0395, Japan*
[e]*Pan-Omics Data-Driven Research Innovation Center, Kyushu University, Fukuoka 816-8580, Japan*
[f]*Department of Materials Science and Engineering, Virginia Tech, Blacksburg, VA 24061, USA*
[g]*Reactor Materials and Mechanical Design Group, Energy and Environmental Directorate, Pacific Northwest National Laboratory, WA 99352, USA*
† Electronic supplementary information (ESI) available. See DOI: **https://doi.org/10.1039/d3nr00992k**

observation using transmission electron microscopy (TEM) has attracted great interest.[14–18] TEM observation with simultaneous heating directly reveals morphological changes in the nanoscale; therefore, *in situ* observation is performed to clarify the sintering behaviour mostly in two-dimensional (2D) cases. However, three-dimensional (3D) plus time, namely 4D, imaging technique would be informative as has been reported by applying the X-ray tomography technique.[19–21] The spatial resolution of X-ray tomography is up to several tens of nanometres[20] to date. Thus, TEM observation is necessary to quantitatively investigate the sintering behaviour of NPs. Additionally, because the NPs are not always in regular/uniform shape[22,23] and easy to aggregate, more than two NPs are likely overlapped along the electron beam projection-direction, making conventional 2D-based observation sometimes inadequate for analysing the sintering. Therefore, implementing a 4D analysis by integrating the *in situ* observation and electron tomography (ET)[24,25] would deepen our experimental-based understanding of nanoscale sintering behaviour.

There have also been numerous attempts using computational science.[26] Because atomistic scale simulation can provide intuitive insights, nanoscale sintering mechanisms have been studied in great detail. Molecular dynamics (MD) simulation is a powerful tool for visualizing an atomic flow during sintering and has revealed nanoscale characteristic behaviour.[11,27,28] Although the time duration of MD simulation is basically femto second scale, a larger temporal scale simulation is required to predict the sintering behaviour of NP ensemble systems for industrial application. For this purpose, the continuous model, such as phase-field simulation,[29,30] is one of the most ideal methods. However, some parameters, and sometimes also incorporating models, are empirically determined by a researcher's intuition to fit reference experiments. This subjective part has no guarantees of the predictive accuracy of the sintering behaviour beyond the time scale or temperature range set in the reference experiments. The overfitting may be resolved using recently emerged numerical approaches, *i.e.*, integrating with experimental data, called data assimilation.[31] The data science combined technique can determine the parameters without prior knowledge and hence may give the models robustness. Because of the advent of the data science approach in materials science, the acquisition of 4D experimental data is an important step toward precise modelling for NP sintering.

In this study, we demonstrate the protocol of *in situ* heating as well as its time-resolved 3D observation methods for the sintering of NPs using scanning TEM (STEM). The targeted material is Cu NPs, whose sintering behaviour is highly sensitive to contamination. The contamination comes from not only oxidation but also the adsorption of hydrocarbon molecules induced by electron beam irradiation. Hence, an experimental framework that can handle such NPs needs to be designed and developed first. Thus, this study provides an overview of (1) a newly developed *in situ* heating holder that can instantaneously raise/lower the temperature and transfer NP samples to TEM without exposing the atmosphere and (2) an ultra-low electron dose observation performed to prevent electron beam-induced artefacts. The developed low-dose image processing successfully visualizes the sintering behavior of Cu NPs in 4D, in addition to discussing the sintering behavior of Cu NPs in the nanoscale.

Materials and methods

Sample preparation

Generally speaking, NPs are highly reactive compared to bulk states because of their high surface to volume ratio.[32] To avoid contamination from the atmosphere, we utilized a glove box and a heating TEM holder, equipping an atmospheric isolation function. Fig. 1 shows the equipment used in the sampling process. In the glove box filled with Ar gas, Cu NPs (Mitsui Mining & Smelting Co., Ltd) with an average diameter of 150 nm were first dispersed in ethanol and then dropped onto the Si_3N_4-supported MEMS heating chip (NORCADA), which can raise and lower the temperature with a response time of less than 100 ms. Because the neck growth rate had been discussed in several minutes order in the conventional theories,[8,9] the response time is regarded as instantaneous in this study.

The chip was mounted on Double Tilt 4 Electrodes Transfer Holder (Mel Build). This holder can store samples inside its axis while maintaining its airtightness due to a rubber ring, enabling the transfer of samples to TEM without exposing them to the atmosphere.

To clarify the structure of the Cu NPs, we performed an atomic resolution observation for that sample. Fig. 2(a) shows a bright field (BF)-TEM image of the Cu NPs obtained using Titan Cubed G2 (FEI) operated at an acceleration voltage of 300 kV. By focusing on the surface of NPs, we obtained a high resolution (HR) TEM image, as depicted in Fig. 2(b). The NPs had a core–shell structure, where NPs with an average diameter of 150 nm were covered by crystalline NPs with an average diameter of less than or equal to 10 nm. The fast Fourier transform (FFT) pattern from the surrounding NPs showed spots corresponding to Cu lattice plane distances, meaning that the shell was also a Cu polycrystal. Hereinafter, the core and shell NPs are called NP-150 and NP-10, respectively. Note that the NPs observed here were not used in the 4D observation.

In situ ET observation

In general, the high electron dose likely induces heating of samples that triggers undesirable coalescence of NPs.[33] Other problems, such as beam-induced damage and contamination, can also prevent the observation of sintering behaviour. Therefore, in this study, the extremely low electron dose condition is set to establish an artifact-less experiment.

Tilt-series of high-angle annular dark field (HAADF)-STEM images were acquired using the same equipment as in the previous section. A convergence semi-angle was set to 1.2 mrad. The image size was 1024 × 1024 pixels (1.04 nm per pixel), and the dwell time was 500 ns per pixel. The tilt angle was changed

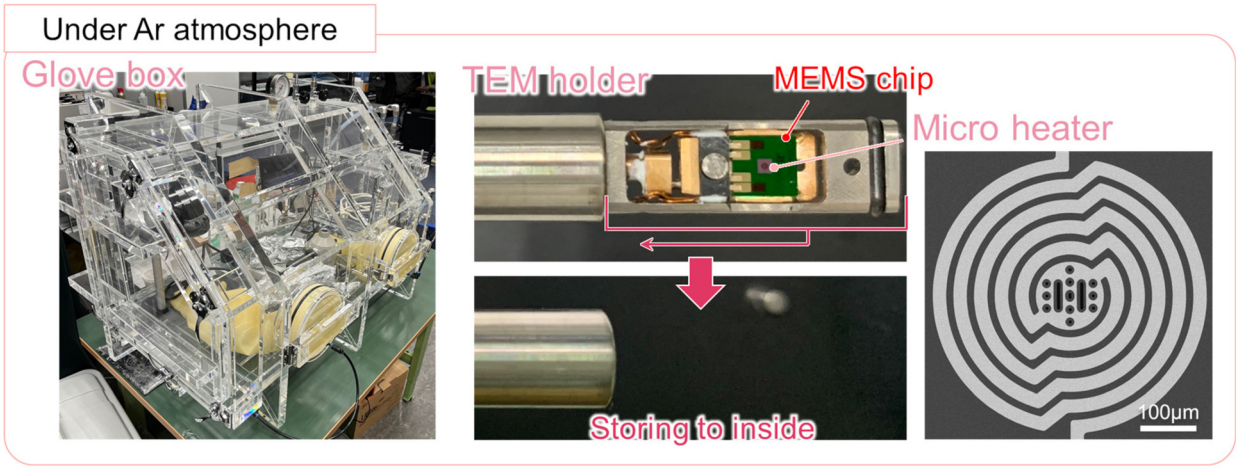

Fig. 1 Photographs of the sample preparation/transfer/heating system employed in this study. All the sample preparation was performed in an Ar gas-filled glove box (left). The newly designed MEMS-based *in situ* heating holder carries a sample while maintaining air tightness (middle). Copper NPs were dispersed on the micro heater (right).

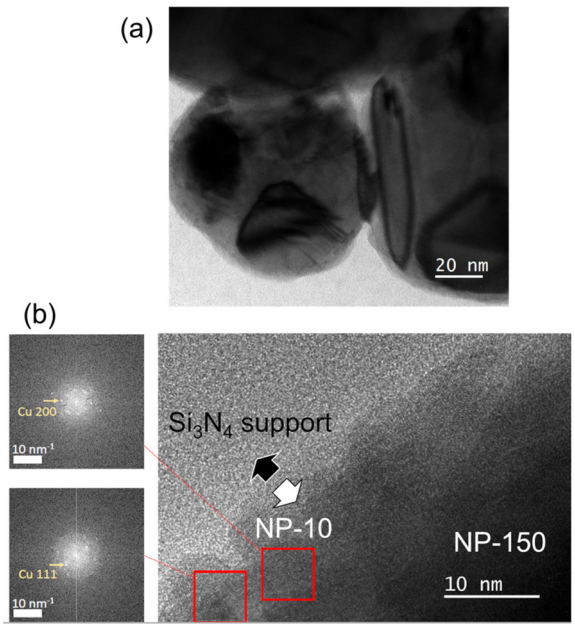

Fig. 2 TEM images of Cu NPs used in this study. (a) A BF-TEM image showing entire shape of NPs. (b) A HRTEM image focusing on the shell of NPs. FFT patterns from the shell are also shown.

in the range of −40°–40° with an increment of 2°. Therefore, 41 images were obtained in one tilt-series. The probe current was set to 2.0 pA. The elementary charge is defined as $1e^- = 1.6 \times 10^{-19}$ C. With these parameters, the total number of incident electrons used for one tilt-series can be calculated as follows: (Probe current in a unit of e^-) × (Exposure time per frame) × (The number of images per tilt-series), where the electrons passing through only the Si_3N_4 support film were also included. From the above equation, the total number of incident electrons and the electron dose were calculated to be 2.7×10^8 e^- and 250 e^- nm^{-2}, respectively. This total number of incident electrons is almost half of the generally recognized ultra-low dose TEM tomography imaging with a direct electron detection camera.[34] Notably, the HAADF-STEM signal is weaker than that of BF-TEM. Because the HAADF-STEM signal is basically free from diffraction, *i.e.*, the signal intensity purely reflects the projection of targets, this study employed it. Notably, the tolerable electron doses for biological samples ever reported are, for example, 5000–10 000 e^- nm^{-2} (frozen bacterium)[35] and 1000 e^- nm^{-2} (uranyl acetate-stained catalase).[36]

Fig. 3 shows a summary of the heating conditions. The sample was heated at 200 °C for 1 h to prevent beam-induced contamination before the observation. Without the process,

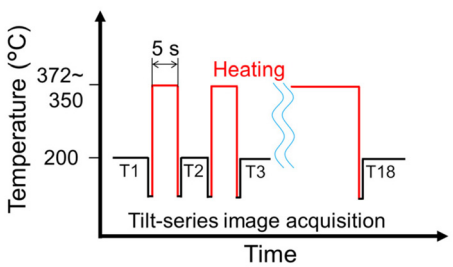

Tilt-series No.	Total time on PT (s)	Temperature (°C)	Tilt-series No.	Total time on PT (s)	Temperature (°C)
T1	0	372	T10	46	372
T2	5	370	T11	51	370
T3	12	370	T12	61	364
T4	17	370	T13	71	364
T5	22	370	T14	81	364
T6	27	372	T15	100	354
T7	31	372	T16	120	353
T8	36	370	T17	150	351
T9	41	370	T18	209	350

Fig. 3 Schematic diagram illustrating the heating process. Because the heating TEM holder can instantaneously increase or decrease the sample temperature, images can be acquired at a standby temperature (ST) immediately after each heating step.

the Cu NPs did not show sintering probably owing to the contamination, as shown in Fig. S1.† During the acquisition of all the tilt-series images, the Cu NPs were also maintained at 200 °C to successfully perform the experiment. Notably, the sintering progress was not recognized at 200 °C, while the obvious progress was observed after the temperature was set to 350 °C, as shown in a subsequent section. Hereinafter, the setting temperatures of 200 °C and 350 °C are called "standby temperature (ST)" and "processing temperature (PT)", respectively. Overshooting from the setting temperature was recognized, and the median temperature is shown in Fig. 3. The PT was initially maintained at around 5 s, and later, the time was extended until the sintering proceeded. After sintering was observed, the temperature was lowered to the ST, and one tilt-series was acquired. We repeated this procedure until the total PT time reached 209 s. The details of the heating log are shown in Fig. S2.† In this study, a total of 18 time series were obtained. Although the response time of the MEMS chip was less than 100 ms, the sampling interval of the used software was 1 s. This study regarded the time on PT as the interval between 0.5 s before the time when the PT was recorded and 0.5 s after the time that started to decrease from the PT. Therefore, the PT time obtained in each PT step contained an error of ±1 s.

Image processing

Fig. 4(a) shows the flow chart of the image processing procedure. The obtained tilt-series images were first denoised using BM3D (block matching 3D)[37] whose parameters had been optimized, so the peak-signal-to-noise-ratio between a raw image and its 50-frame-averaged one (reference image) became maximum, as shown in Fig. 4(b). The parameters, noise type and variance were chosen as "g4" and 137, respectively. This denoising technique successfully recovered the signal intensity of the low-electron dose images, as shown in Fig. S3.† To align the images so that they have a common tilt axis, MATLAB implemented an image registration tool, in which the optimizer and the metrics were set to (1 + 1) evolutionary strategy[38] and Mattes mutual information,[39] respectively. The image deviation in each tilt-series was corrected so that the NP positions accurately overlap between image pairs with adjacent tilt angle values. After the image registration, we determined the position of the tilt axis using the simple back projection images, as shown in Fig. 4(c). The axis position was chosen so that the artefact of the particles in the stacked back projection images became small. For the 3D reconstruction, because the tilt angle range was limited to ±40° in this study, the artefact that comes from the limited tilt angle, called missing wedge,[25] was expected. Therefore, the compressed sensing implemented algorithm, ISER (iterative series reduction),[40,41] was employed to decrease the missing wedge, as illustrated in Fig. S4.† The ISER utilizes a fast convergence algorithm and reconstructs an object from the measured projection data by minimizing the total variation norm while maintaining data fidelity. The reconstruction is iteratively performed; in each step, the reconstruction error is first reduced, and then the total variation norm is reduced. This procedure continues for given iteration times. Minimizing the total variation norm leads to less gradation in the reconstructed images, meaning that the uncertainty in the edge of an object resulting from the missing wedge can be reduced. The parameters were set as follows: iteration is 300, application times are 1 × 1, and sensitivity is 1. The reconstructed tomograms were binarized by applying Otsu's method after 3D reconstruction. Finally, the tomograms were processed by eroding and dilating for the restoration of image texture ununiformity, which was caused by the 3D reconstruction process.

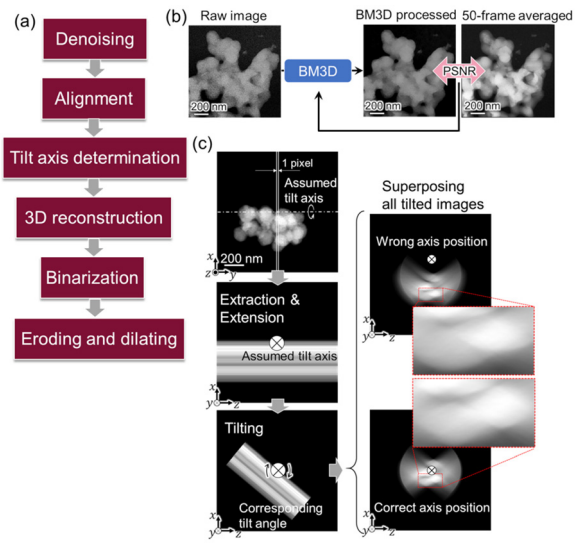

Fig. 4 Flow chart of image processing procedure with some specific details. After each tilt-series image acquisition, the images were processed by following the procedure shown in (a). (b) The parameters of BM3D filter were optimized using additionally acquired raw image and its 50-frame averaged image. (c) The tilt axis for each tilt-series was determined by creating ray images and optimizing the axis position, which effectively reduced artefact.

Results and discussion

In situ observation in 2D

Before showing the 3D sintering behaviour, herein, we demonstrate 2D *in situ* observation results focusing on neck formation between the NPs. Fig. 5 shows the BF-TEM images of NPs heated at the temperature and time, which are indicated on the upper left of each image. The gap between the NP-150 cores was filled with the NP-10 shell as the heating continued. Finally, the neck was clearly formed. The sintering mechanism at the initial stage of the Cu NPs used in this study was mainly dominated by the diffusion of the NP-10 shell around the NP-150 cores. The crystal orientation of NP-10 is probably random. Therefore, even if there is crystal orientation dependence in the sintering mechanism, its effect is negligibly small, especially at the initial stage; the presence of NP-10 may further reduce or conceal such dependence. It is noteworthy

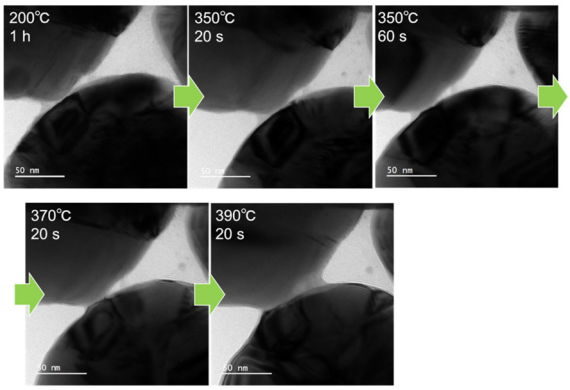

Fig. 5 2D *in situ* observation of Cu NPs. The sintering was proceeded predominantly by the diffusion of NP-10.

that neither particle rotation nor chemical reaction with the Si_3N_4 support was recognized in this BF-TEM observation. Thus, the 4D observation performed in this study under extremely reduced electron dose conditions was also free from such artefacts.

3D morphology of sintering NP system with a bimodal size distribution

Fig. 6 demonstrates the 3D sintering behaviour of NPs at representative times. The figure clearly shows the neck formation and growth with the proceeding of the sintering time. Although this study repeatedly continued temperature shifts between ST and PT, no significant differences in sintering progress were recognized from the case of continuous heating, as shown in Fig. S5.† In addition, the 3D reconstruction artefacts, *e.g.*, streaks along with the tilt direction, were not identified. Therefore, the alignment of the NP position described in the "image processing" was successfully performed, meaning that the morphological change due to the electron beam irradiation is negligibly small. Little neck growth was observed after the PT time of 60 s in this study. The 3D morphologies at other sintering times are shown in Fig. S6.†

Neck growth evaluation

One of the benefits of 3D reconstruction is enabling the precise measurement of particle position and shape, even if the NPs aggregate and are difficult to distinguish from each NP in a 2D view. Generally speaking, during sintering, the neck grows, and the distance between two adjacent NPs decreases (densification). The neck width and distance are important factors in quantifying the sintering state. In this study, the sintering behaviour was evaluated by measuring these parameters, including those describing particle shape from the seven NP pairs shown in Fig. 7. Briefly, the descriptors we used were the neck width, the distance measured from the three directions, particle radius, and aspect ratio of the NPs. The details of the measurement process are described in the next paragraph.

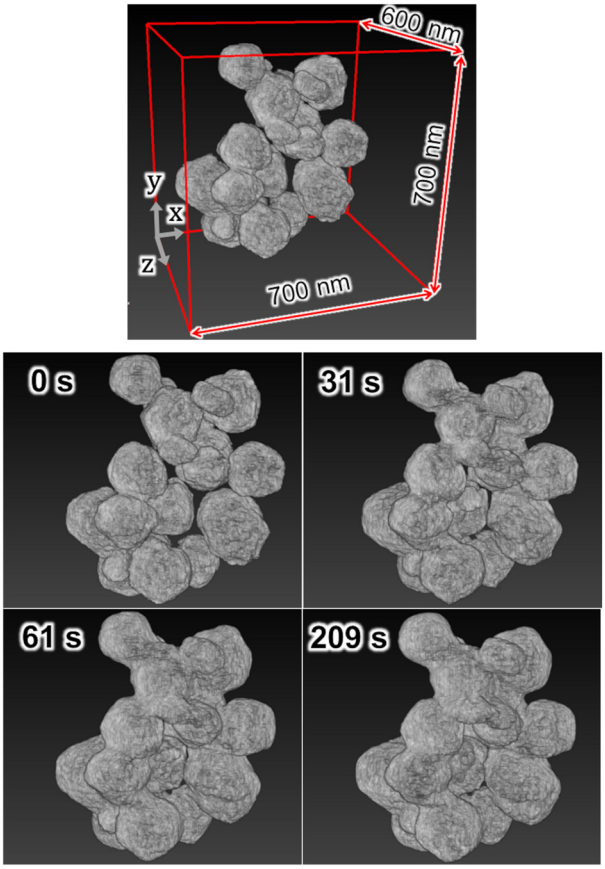

Fig. 6 Changes in 3D morphology of NPs during the sintering (heating) process. The neck growth and densification were clearly observed during the sintering time. In this study, there were no significant changes above 60 s. Note that the obtained data were averaged in the range of 3 × 3 × 3 pixels (30.4 nm^3) for visibility.

First, a rectangular section containing a great circle of two neighbouring NPs was extracted, centring on the section where the longest neck width appeared (surrounded by the yellow solid line depicted in Fig. 7 lower left). Then, the extracted tomograms were projected along the *z*-axis. The created image includes the maximum width, height and neck width of the targeted NPs. Thus, it can be utilized to measure the neck radius r_n, which is half of the neck width W_n, the distance between the centre of mass (COM) for each NP in the *x*–*y* plane (d_{xy}), the representative particle radius r_p, and the representative NP's aspect ratio H/W, after trimming the other NPs and binarization, as shown in Fig. 7 lower right. Note that this study assumed that the density was constant throughout the NPs; therefore, the COM was calculated using binarized images. In the trimming process, the NPs that did not form the necks with the targeted NP pair were eliminated as they were, and those that formed the neck were divided at the necks and removed from the extraction box, as shown in Fig. S5.† Furthermore, d_z is defined as the distance of the COM in the *z*-direction and utilized with d_{xy} to calculate the distance between the NP pair (d) as the equation displayed in Fig. 7 lower left. Note that the COM in the *z*-direction was measured by averaging the minimum and

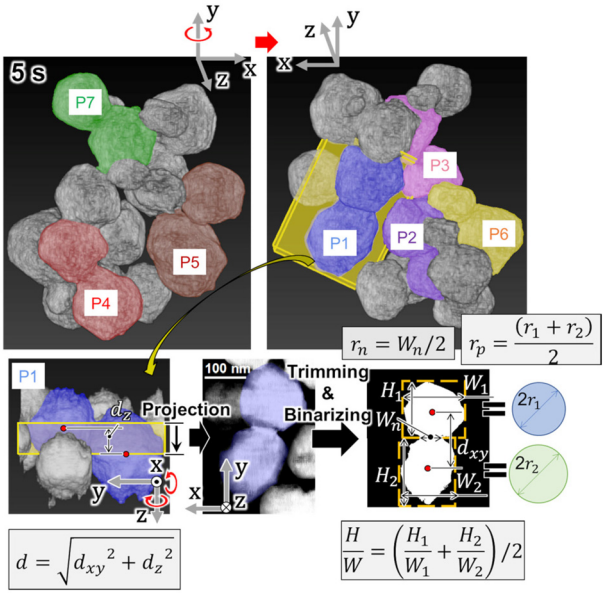

Fig. 7 Schematic drawing illustrates the measurement process of d, r_p, r_n, and H/W in targeted NPs. A section of targeted NPs was first extracted. Then, NPs around the targeted NPs in the extracted section were trimmed by applying the method shown in Fig. S5.† The trimmed image was binarized to obtain the parameters. Here, d_{xy} and d_z are the distance between the centre of mass (COM) of targeted NPs in x–y plane and z-direction, respectively. The radius of each particle (r_1 and r_2) was calculated by approximating the targeted NPs to circles of equal area.

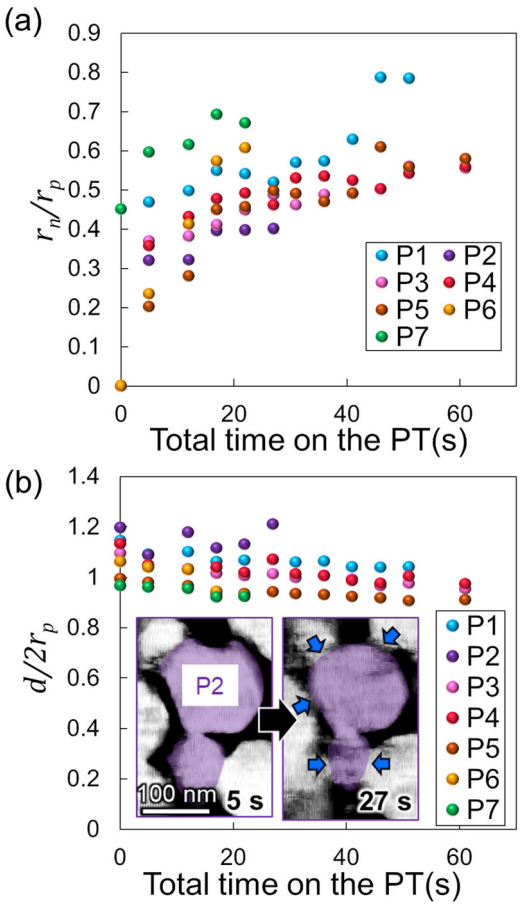

Fig. 8 Morphological changes in NPs as a function of the PT. (a) The variation in the neck width and (b) changes in the COM of the targeted NP pairs, with the PT time.

maximum z-coordinates in each NP. r_p is defined as the average radius, where each radius is obtained from a circle whose area is equal to the extracted tomograms. H/W is calculated by averaging each aspect ratio.

We measured the geometrical parameters up to 60 s of the PT time, where significant neck growth was confirmed to cease. Fig. 8(a) and (b) demonstrate the variation in neck radius and distance between NPs, which are normalized by the particle radius and diameter, respectively. In some NP pairs, the measurement was interrupted because the other adjacent NPs moved to the pair and coalesced with them, making it difficult to distinguish the original pair. As depicted in Fig. 8(a) and (b), most NP pairs increased the neck width with proceeding PT time, whereas the particle distance decreased. However, P2, which has the largest distance among the seven, demonstrated the fluctuation in the distance variation, as shown in Fig. 8(b). The variation was because the NPs showed sintering with the other adjacent NPs, as illustrated by blue arrows in Fig. 8(b), inhibiting the densification between the targeted pair. Such many-body-effect yielded abnormal variation among the seven. The difficulty in theoretically predicting the sintering behaviour of an NP pair in an NP-many-body system arises from sintering with other NPs, meaning it is difficult to predict; for example, neck growth from a two-sphere model is commonly used in classical models.[6–8] Notably, the neck growth was faster and occurred at a relatively lower temperature compared to the case of micron-sized Cu particles,[8] where 100 μm particles took more than 10 minutes to reach about $r_n/r_p = 0.3$ when 1050 °C, while the NPs reached a larger neck width in several tens of seconds with 350 °C, as shown in Fig. 8(a). The rapid neck growth at low temperatures is an NP-specific phenomenon, likely originating from the high surface-to-volume ratio; significantly high surface tension mainly drives the sintering.[6]

Fig. 9(a) shows the plots of the neck radius and the distance, where the measured H/W are also indicated. In the figure, the dashed line represents a model case that is derived by assuming that contact spheres form a cylindrical neck while preserving total volume, as illustrated in Fig. 9(b). The analytical expression is demonstrated in Fig. S6.† As expected, the neck radius and the distance clearly show a negative correlation in all the NP pairs except P2. The relationship is almost monotonous and corresponds to densification; it is commonly observed in the sintering process, as also illustrated in the dashed line in Fig. 9(a). The NP pairs with smaller H/W shows smaller distance, whereas those with larger H/W shows larger distance. This order in the figure is intuitively understandable because the distance likely depends on the particle shape, *i.e.*, the flattened NP pair has a smaller distance, whereas the vertically elongated NP pair has a larger one, as schematically demonstrated in Fig. 9(c).

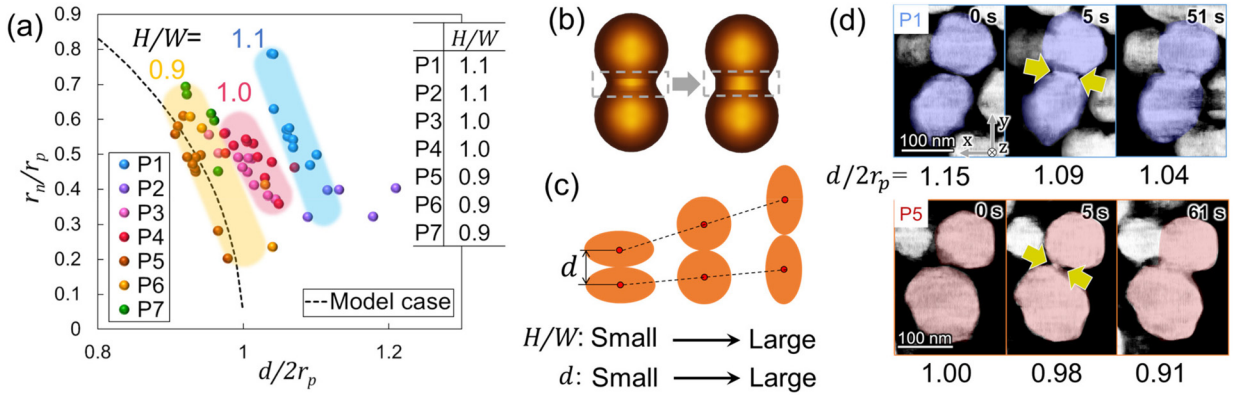

Fig. 9 A summary of the targeted NP's morphology variation. (a) The relationship between the neck width and the COM distance while considering the aspect ratio of each of targeted NP pairs. Note that because of the arbitrariness of the initial position of NPs, the results at r_n = 0, *i.e.*, prior to neck formation, were not included. (b) Simplified sintering model employed to calculate the dashed line in (a). (c) Schematic illustrating the relationship between the aspect ratio and the COM distance. (d) Representative 2D projection images utilized for the neck growth and the distance measurement.

It is noteworthy that the sintering proceeded even if $d/2r_p$ was more than or equal to 1 when H/W = 1, *i.e.*, the sintering occurred in NP pairs that were not apparently in touch at the beginning. The apparent nanoscale gap is due to the presence of an NP-10 shell. Because the NP-10 shell was not dense, the signal intensity from the shell was much lower than that from the NP-150 cores, resulting in the invisibility of the NP-10 shell after binarization. Fig. 9(d) demonstrates the representative sintering behaviour in this study. The separated NP on the lower side of P1 moved toward the neighbouring NP, resulting in the formation of the neck in only 5 s. In P5, however, the NP pair initially formed a thin neck with only small changes in the distance. The neck grew in several tens of seconds, followed by bridge formation. Notably, the neck formed at the initial stage was not visible in the tomograms because of the low signal intensity of the NP-10 shell. The neck likely appeared when it grew and had sufficient thickness. In P1, the invisible neck may have already formed at the initial stage. Densification occurred while growing the neck, resulting in apparent particle motion.

The developed procedure in this study visualizes the nanoscale variation even if the NPs are in the many-body-system. Most of the interfaces of the NPs are difficult to observe in 2D because particles tend to physically overlap each other along the projection direction, and the need for 3D observation increases in practical cases, such as the analysis of industrial products.

Conclusions

The ultra-low electron dose observation and the novel MEMS-based *in situ* heating holder made it possible to observe the nanoscale sintering behaviour. The BM3D-based noise filtering approach and the compressed sensing-aided-3D reconstruction algorithm compensated for the low signal-to-noise ratio due to the ultra-low electron dose and the 3D reconstruction artefact due to the limited tilt angle range, respectively. These image processing techniques help to visualize the nanoscale sintering behaviour clearly in 4D space–time while reducing artefacts to an uninfluential level. The neck width and the distance between the Cu NP pairs of interest were evaluated to determine the sintering behavior. These two factors always showed a monotonous negative correlation depending on their aspect ratio if there were few bindings with other NPs. The apparently separated NPs also showed sintering because the shells of NPs, which were invisible in the reconstructed tomograms due to their sparse distribution, formed the nanoscale bridging at the initial stage of sintering. Such sintering initiation highly contributed to NP sintering.

To precisely predict nanoscale dynamics, 4D datasets could also be utilized as experimental inputs for computational modeling or data science approaches, such as data assimilation. Furthermore, 4D electron microscopy is an essential fundamental insight for such a sophisticated computational science, leading to a de-facto standard for revealing unexplored physics in nanoscale.[42]

Author contributions

H. Saito, S. Hata and M. Murayama designed the project. H. Miyazaki developed the TEM holder for this study. S. Hata prepared the sample. K. Wada and H. Saito carried out the observation. M. Yoshinaga, S. Ihara, and H. Saito performed the image processing. M. Yoshinaga, S. Ihara, H. Saito, and M. Murayama wrote the draft of this paper. All the authors participated in the discussion and approved the paper.

Conflicts of interest

There are no conflicts to declare.

Acknowledgements

This study was supported by JSPS KAKENHI Grant Number (JP18H05479, JP20H02426, JP20K21093, JP21K20491, JP 22K14466), Iketani Science and Technology Foundation, CREST Nanomechanics (JPMJCR1994), Japan Science and Technology Agency (JST) CREST (JPMJCR18J4), and Five-Star Alliance. This study was partly supported by Nano-scale Characterization and Fabrication Laboratory (NCFL), Institute for Critical Technology and Applied Science (ICTAS), Virginia Tech and used shared facilities at the Virginia Tech National Center for Earth and Environmental Nanotechnology Infrastructure (NanoEarth), a member of the National Nanotechnology Coordinated Infrastructure (NNCI), supported by NSF (ECCS 2025151).

References

1 M. Rahaman, *Ceramic processing*, CRC Press, 2007.
2 A. Kamyshny and S. Magdassi, *Small*, 2014, **10**, 3515–3535.
3 Y. Kamikoriyama, H. Imamura, A. Muramatsu and K. Kanie, *Sci. Rep.*, 2019, **9**, 899.
4 H. Imamura, Y. Kamikoriyama, A. Muramatsu and K. Kanie, *Sci. Rep.*, 2021, **11**, 24268.
5 S. Khan, L. Lorenzelli and R. Dahiya, *IEEE Sens. J.*, 2015, **15**, 3164–3185.
6 J. Perelaer, P. Smith, D. Mager, D. Soltman, S. Volkman, V. Subramanian, J. Korvink and U. Schubert, *J. Mater. Chem.*, 2010, **20**, 8446–8453.
7 G. Kuczynski, *J. Appl. Phys.*, 1949, **20**, 1160–1163.
8 W. Kingery and M. Berg, *J. Appl. Phys.*, 1955, **26**, 1205–1212.
9 R. Coble, *J. Am. Ceram. Soc.*, 1958, **41**, 55–62.
10 M. Ashby, *Acta Metall.*, 1974, **22**, 275–289.
11 P. Zeng, S. Zajac, P. Clapp and J. Rifkin, *Mater. Sci. Eng., A*, 1998, **252**, 301–306.
12 J. Shi, Y. Deguchi and Y. Sakabe, *J. Mater. Sci.*, 2005, **40**, 5711–5719.
13 Z. Fang, H. Wang and V. Kumar, *Int. J. Refract. Met. Hard Mater.*, 2017, **62**, 110–117.
14 Y. Chen, R. Palmer and J. Wilcoxon, *Langmuir*, 2006, **22**, 2851–2855.
15 M. Asoro, P. Ferreira and D. Kovar, *Acta Mater.*, 2014, **81**, 173–183.
16 W. Yuan, D. Zhang, Y. Ou, K. Fang, B. Zhu, H. Yang, T. Hansen, J. Wagner, Z. Zhang, Y. Gao and Y. Wang, *Angew. Chem.*, 2018, **130**, 17069–17073.
17 M. Asoro, D. Kovar, Y. Shao-Horn, L. Allard and P. Ferreira, *Nanotechnology*, 2010, **21**, 025701.
18 S. Tsyganov, J. Kästner, B. Rellinghaus, T. Kauffeldt, F. Westerhoff and D. Wolf, *Phys. Rev. B: Condens. Matter Mater. Phys.*, 2007, **75**, 045421.
19 F. Xu, X. Hu, H. Miao and J. Zhao, *Opt. Lasers Eng.*, 2010, **48**, 1082–1088.
20 J. Villanova, R. Daudin, P. Lhuissier, D. Jauffrès, S. Lou, C. Martin, S. Labourè, R. Tucoulou, G. Martìnez-Criado and L. Salvo, *Mater. Today*, 2017, **20**, 354–359.
21 A. Kondarage, G. Poologasundarampillai, A. Nommeots-Nomm, P. Lee, T. Lalitharatne, N. Nanayakkara, J. Jones and A. Karunaratne, *J. Am. Ceram. Soc.*, 2022, **105**, 1671–1684.
22 H. Vanrompay, E. Bladt, W. Albrecht, A. Béché, M. Zakhozheva, A. Sánchez-Iglesias, L. Liz-Marzán and S. Bals, *Nanoscale*, 2018, **10**, 22792–22801.
23 T. Altantzis, I. Lobato, A. Backer, A. Béché, Y. Zhang, S. Basak, M. Porcu, Q. Xu, A. Sánchez-Iglesias, L. Liz-Marzán, G. Tendeloo, S. Aert and S. Bals, *Nano Lett.*, 2019, **19**, 477–481.
24 W. Albrecht and S. Bals, *J. Phys. Chem. C*, 2020, **124**, 27276–27286.
25 J. E. Frank, *Electron tomography: methods for three-dimensional visualization of structures in the cell*, Springer, 2010.
26 P. Grammatikopoulos, M. Sowwan and J. Kioseoglou, *Adv. Theory Simul.*, 2019, **2**, 1900013.
27 H. Zhu and R. Averback, *Philos. Mag. Lett.*, 1996, **73**, 27–33.
28 J. Nandy, N. Yedla, P. Gupta, H. Sarangi and S. Sahoo, *Mater. Chem. Phys.*, 2019, **236**, 121803.
29 V. Kumar, Z. Fang and P. Fife, *Mater. Sci. Eng. A*, 2010, **528**, 254–259.
30 J. Hötzer, M. Seiz, M. Kellner, W. Rheinheimer and B. Nestler, *Acta Mater.*, 2019, **164**, 184–195.
31 A. Yamanaka, Y. Maeda and K. Sasaki, *Mater. Des.*, 2019, **165**, 107577.
32 L. Xu, H. Liang, Y. Yang and S. Yu, *Chem. Rev.*, 2018, **118**, 3209–3250.
33 A. Surrey, D. Pohl, L. Schultz and B. Rellinghaus, *Nano Lett.*, 2012, **12**, 6071–6077.
34 V. Migunov, H. Ryll, X. Zhuge, M. Simson, L. Strüder, K. Batenburg, L. Houben and R. Dunin-Borkowski, *Sci. Rep.*, 2015, **5**, 14516.
35 L. Kourkoutis, J. Plitzko and W. Baumeister, *Annu. Rev. Mater. Res.*, 2012, **42**, 33–58.
36 R. Glaeser, *J. Ultrastruct. Res.*, 1971, **36**, 466–482.
37 K. Dabov, A. Foi, V. Katkovnik and K. Egiazarian, *IEEE Trans. Image Process.*, 2007, **16**, 2080–2095.
38 M. Styner, C. Brechbühler, G. Székely and G. Gerig, *IEEE Trans. Med. Imaging*, 2000, **19**, 153–165.
39 S. Raghunathan, D. Stredney, P. Schmalbrock and B. Clymer, *13th Annu. Med. Meets Virtual Reality Conf. (MMVR)*, 2005.
40 K. Kamo, N. Horii, H. Furukawa and H. Kudo, *Microscopy*, 2015, **64**, i84.
41 H. Kim, K. Sadataka and H. Kudo, ICBIP 21: Proceedings of the 6th International Conference on Biomedical Signal and Image Processing, 2021, 65–71.
42 S. Spurgeon, C. Ophus, L. Jones, A. Petford-Long, S. V. Kalinin, M. J. Olszta, R. E. Dunin-Borkowski, N. Salmon, K. Hatter, W.-C. D. Yang, R. Sharma, Y. Du, A. Chiaramonti, H. Zheng, E. C. Buck, L. Kovarik, R. L. Penn, D. Li, X. Zhang, M. Murayama and M. L. Taheri, *Nat. Mater.*, 2021, **20**, 274–279.